Acta Biomaterialia 80 (2018) 188–202

Contents lists available at ScienceDirect

Acta Biomaterialia

journal homepage: www.elsevier.com/locate/actabiomat

Full length article

Stiffness memory nanohybrid scaffolds generated by indirect 3D printing for biologically responsive soft implants

Linxiao Wu [a], Jatinder Virdee [a], Elizabeth Maughan [b], Arnold Darbyshire [a], Gavin Jell [a], Marilena Loizidou [a], Mark Emberton [a], Peter Butler [b,c], Ashley Howkins [d], Alan Reynolds [d], Ian W. Boyd [d], Martin Birchall [b], Wenhui Song [a,*]

[a] UCL Centre for Nanotechnology and Regenerative Medicine, Division of Surgery & Interventional Science, University College London, London NW3 2PF, UK
[b] UCL Ear Institute, Royal National Throat Nose and Ear Hospital and University College London, London, UK
[c] Department of Plastic and Reconstructive Surgery, Royal Free London NHS Foundation Trust, London NW3 2PF, UK
[d] Experimental Technique Centre, Brunel University London, UB8 3PH, UK

ARTICLE INFO

Article history:
Received 9 May 2018
Received in revised form 13 September 2018
Accepted 13 September 2018
Available online 15 September 2018

Keywords:
Stiffness memory
3D-TIPS
3D printing
Phase separation
Polyurethane nanohybrid
Soft implants

ABSTRACT

Cell and tissue stiffness is an important biomechanical signalling parameter for dynamic biological processes; responsive polymeric materials conferring responsive functionality are therefore appealing for *in vivo* implants. We have developed thermoresponsive poly(urea-urethane) nanohybrid scaffolds with 'stiffness memory' through a versatile 3D printing-guided thermally induced phase separation (3D-TIPS) technique. 3D-TIPS, a combination of 3D printing with phase separation, allows uniform phase-separation and phase transition of the polymer solution at a large interface of network within the printed sacrificial preform, leading to the creation of full-scale scaffolds with bespoke anatomical complex geometry. A wide range of hyperelastic mechanical properties of the soft elastomer scaffolds with interconnected pores at multi-scale, controlled porosity and crystallinity have been manufactured, not previously achievable via direct printing techniques or phase-separation alone. Semi-crystalline polymeric reverse self-assembly to a ground-stated quasi-random nanophase structure, throughout a hierarchical structure of internal pores, contributes to gradual stiffness relaxation during *in vitro* cell culture with minimal changes to shape. This 'stiffness memory' provides initial mechanical support to surrounding tissues before gradually softening to a better mechanical match, raising hopes for personalized and biologically responsive soft tissue implants which promote human fibroblast cells growth as model and potential scaffold tissue integration.

Statement of Significance

Biological processes are dynamic in nature, however current medical implants are often stronger and stiffer than the surrounding tissue, with little adaptability in response to biological and physical stimuli. This work has contributed to the development of a range of thermoresponsive nanohybrid elastomer scaffolds, with tuneable stiffness and hierarchically interconnected porous structure, manufactured by a versatile indirect 3D printing technique. For the first time, stiffness memory of the scaffold was observed to be driven by phase transition and a reverse self-assembly from a semicrystalline phase to a quasi-random nanostructured rubber phase. Early insight into cell response during the stiffness relaxation of the scaffolds *in vitro* holds promise for personalized biologically responsive soft implants.

1. Introduction

Living tissues constantly remodel throughout life in response to changes in mechanical stresses [1,2] or injury [3,4]. Changes in cellular and extracellular matrix (ECM) stiffness, in response to dynamic mechanical signalling, play a critical role in diverse physiological and pathological processes including cell motility [5–8], migration [9–12], proliferation [7,13] stem cell differentiation [5,14–16] and vascular disease [17,18]. However, the biomechanical factors which contribute to soft tissue development and maintenance are not fully understood. Tissue engineering is the

* Corresponding author.
E-mail address: w.song@ucl.ac.uk (W. Song).

https://doi.org/10.1016/j.actbio.2018.09.016
1742-7061/

combination of cells with 'scaffold' structures to produce a viable and self-sustaining tissue replacement construct [19,20]. Engineered scaffolds or implants may be regarded as ECM analogues and as such should direct desirable cell behaviour within a given geometrical framework in addition to supplying structural support [21]. Optimization of the scaffold's biomechanical properties, surface chemistry and microarchitecture are vital in conferring this functionality [5,22,23]. Clinically available synthetic scaffolds and implants are manufactured from a limited repertoire of biomaterials. Although these materials have established track records of long-term mechanical stability and passive structural support, they are often stronger and stiffer than surrounding tissues with little adaptability in response to biological and physical stimuli. In particular, the mechanical mismatches at the interface between the scaffold and native tissue, which determines the long-term integration of implants [5,24,25], can stimulate tissue remodelling, resulting in undesirable clinical outcomes such as stress shielding, extrusion of implants or organ failure [24,26].

In response to these issues, a variety of responsive polymeric materials have been developed for tissue engineering, drug delivery and medical devices. The controlled elastic modulus of polyacrylamide gels, their derivatives, polyethylene glycol hydrogel [12,27–30] and other biological hydrogels [5,31] through chemical cross-linking, have been widely used as model to study stiffness effects in cell cultures. However, they are still constrained by its coupling effect of molecular structural change and elasticity, which often has a narrow range of tunable stiffness. Block-copolymers, such as polyurethane (PU) elastomers, can demonstrate a wide range of tuneable physical and mechanical properties without changes to their underlying molecular structure [32,33] simply by varying the method of self-assembly (i.e. physical phase transition, phase-separation) [34], apart from chemical modification of chain block ratios [35]. Their elasticity and biocompatibility [36] allows for the creation of a diverse family of high-performance polymers composed of various soft and hard segments with unique nano- and microstructures, many of which have been employed in various medical devices and soft implants. In particular, poly(urea-urethane) (PUU) has long demonstrated outstanding compliance, fatigue resistance, biocompatibility and biostability in long-term implantable cardiovascular devices due to its stronger hydrogen chain bonding via urea groups [37,38]. Some PUs have also 'shape memory' – the capability of fixing a temporary shape and recovering to a permanent shape triggered via phase transition, e.g. glass transition or melting temperature, in response to environmental stimuli [37,39]. The hard segment domains within PU chains, which act as reinforcement or confinement, are often responsible for the permanent shape, while the soft segments, with the ability to soften past a certain transition temperature, are responsible for the temporary shape. The biomedical applications and related patents of active implantable devices based on shape-memory polymers (SMPs) have been comprehensively reviewed [40]. Newly FDA approved SMP foam embolization system is claimed to improve a variety of vascular complications [41].

Various fabrication processes have been explored to improve these specifications including thermal induced phase-separation (TIPS), particulate leaching, powder sintering, and freeze drying [42–45]. One general limitation of these techniques is the lack of control over desired uniform pore aperture and size, particularly in the larger complex constructs. The advent of 3D printing has presented the biomedical community with the opportunity to design and manufacture complex 3D organ-like shapes with well-defined macroscopic porous architectures based on patient-specific dimensions (e.g. from X-Ray, computerised tomographic (CT) and magnetic resonance imaging (MRI) scans), without the need for conventional tooling or moulding [46,47]. Printing stimuli-responsive materials will create dynamic 3D structures that can transform their shapes or behaviour under various stimuli [48,49]. Despite this promise, the main caveat for biomedical applications lies in the limitation on the types of biologically active soft biomaterials available for 3D printing. Solution-based PUU cannot be printed and does not easily lend itself to the creation of large porous constructs with complex shape [38,50]. Several methods have been adapted to manufacture polymeric suspension, solution or resin-based scaffolds by using 3D printing combined with freeze-drying [51,52] and indirect 3D printing negative moulding combined with phase separation or in situ crosslinking polymerization [53–55].

Here, we report the manufacture of thermoresponsive PUU nanohybrid scaffolds with 'stiffness memory' using a versatile 3D printing-guided thermally induced phase separation (3D-TIPS) technique. Well-defined micro-channels can be digitally programmed to guide the phase-separation of solution-based PUU, leading to the creation of full-scale scaffolds, with hierarchically interconnected pores and controlled porosity, crystallinity and mechanical properties. We observed stiffness softening to an intrinsic soft rubbery phase at body temperature with maintenance of the preformed complex shape, through reverse self-assembling crossing over a wide range of chain relaxation times. The biological *in vitro* interactions during dynamic mechanical relaxation of these scaffolds demonstrate their promise as personalised and biologically responsive soft scaffolds and implants.

2. Materials and methods

2.1. 3D thermal induced phase-separation (3D-TIPS) manufacturing polyurethane urea scaffolds

Ethylenediamine and polyhedral oligomeric silsesquioxane (POSS) co-terminated poly(urea-urethane (PUU) polymer (PUU-POSS) in N,N-dimethylacetamide (DMAc) solution was synthesised as needed, using methods described previously [38]. The molecular structure of PUU-POSS is illustrated in Scheme 1.

All Polyvinyl alcohol (PVA) preforms for manufacturing and characterisation of PUU-POSS scaffolds were designed in AutoCAD 2014 (Autodesk Inc.), exported as .stl files and transferred to Slic3r software (version 9.9) where they were sliced into an array of consecutive 200 μm layers. The out layers of the preform were kept solid, with all layers in between arranged in an interval orthogonal pattern. The spacing between the PUU-POSS scaffold was governed by the 'infill density', which was varied consecutively from 80% to 30% (with 10% incremental increases). The resulting G-code files were printed using PVA filament of diameter 1.75 mm by an Active X1 fusion deposition modeller (Active 3D Printers Ltd., UK) at 210 °C with X- and Y-printing speed at 150 $mm.s^{-1}$ and Z-printing speed at 25 $mm.s^{-1}$. The printed PVA preform were stored in an airtight desiccator to prevent any structural distortion from absorption of atmospheric humidity.

Each PVA preform was injected with PUU-POSS solution through a surface puncture hole. Three groups of scaffolds were manufactured at different coagulation temperatures and post thermal treatment as described in Table 1. The first group of filled preforms (Cryo Coagulation, CC) were kept overnight at −20 °C and then immersed into deionised ice water for 24 h, with regular water changes at room temperature and subjected to magnetic stirring until the PVA had been dissolved. The second group (Cryo Coagulation + Heating, CC+H) followed the same process of CC group but had additional heat treatment in deionised water at 40 °C for 24 h. The final group (Room temperature Coagulation + Heating, RTC+H) were immersed into deionised water at room temperature (25 °C) and soaked for 24 h, with regular water changes and magnetic stirring, following by heat treatment at

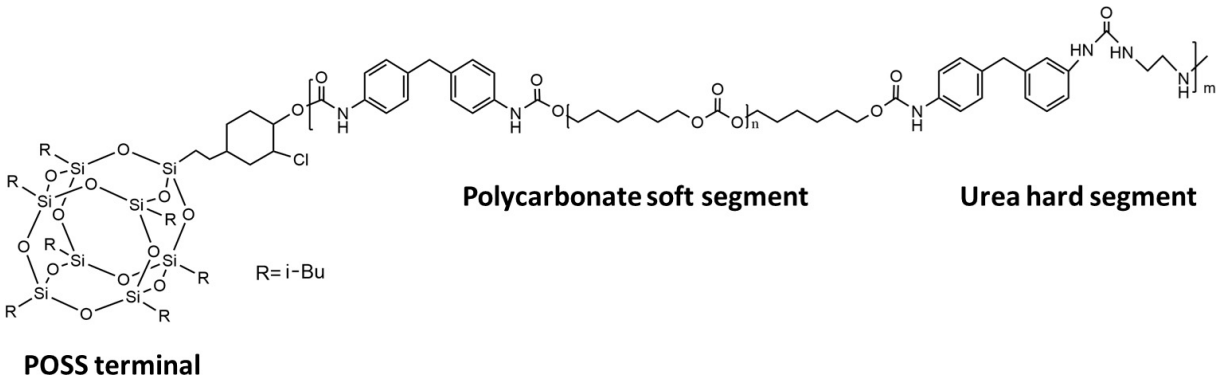

Scheme 1.

Table 1
Process conditions of 3D-TIPS.

Scaffolds	PUU-POSS solution filled PVA preform	Coagulation conditions	Thermal treatment
Room temperature coagulation + heating, RTC+H	Room temperature, 25 °C for 24 h	Room temperature, 25 °C water for 24 h	40 °C water for 24 h
Cryo-coagulation, CC	−20 °C for 24 h	0 °C ice water for 24 h	No thermal treatment
Cryo-coagulation + heating, CC+H	−20 °C for 24 h	0 °C ice water for 24 h	40 °C water for 3 h

40 °C for 24 h until the PVA had been dissolved. FTIR spectroscopy scans showed that after this period of soaking, all PVA had been dissolved from the preforms. All scaffolds were stored in sterile de-ionised water until they were required.

Reconstructed digital .stl file images of an ear and nose were obtained from CT-scan images, sliced with 50% infill density, and printed as PVA preform. PUU-POSS solution was injected into each preform, and the preform washed as outlined for the RTC+H groups above, to produce anatomically shaped polymer scaffolds.

2.2. Static and dynamic mechanical studies

For tensile testing, samples (n = 6; length 60 mm, width 12 mm, thickness 3.5 mm) in wet condition were subjected to uniaxial loads at 5 mm/min using an Instron 5655 tester (Instron Ltd., Norwood, MA, USA) with a 500 N load cell, and ultimate tensile strength, strain at break, tensile modulus and toughness were calculated from load–displacement measurements and averaged. Dynamic mechanical properties of the scaffolds (n = 2; length 15 mm, width 6.5 mm, thickness 2 mm) were tested with a sinusoidal ramp of constant frequency of 1 Hz with a controlled strain (40%) for 200,000 cycles per sample in a bioreactor at 37 °C in water using ElectroForce Biodynamic® Test Instrument 5160 (TA, USA) with a 200 N load cell. Temperature spectra of dynamic tensile mechanical properties of the scaffolds (n = 3, length 60 mm, width 12 mm, thickness 3.5 mm) were tested at wet conditions under the frequency 1 Hz and the strain of 1% at a heating rate of 2 °C/min in the temperature range of −70 to 170 °C for all samples by a dynamic mechanical analysis (DMA) instrument (TA Q800, USA).

2.3. Characterisation of scaffold structure

The phase transitions of the scaffolds were measured from −70 °C to 230 °C using differential scanning calorimeter (DSC Q1000, TA Instrument) at a scan rate of 10 °C/min. The phase structure was further examined by wide-angle X-Ray diffraction (WAXD, Bruker D8 Advance, Germany). The top surfaces and cross sections of dried scaffolds had their surface and cross-sectional features examined at room temperature using an optical microscope (Olympus DSX500, UK) and under a field emission scanning electron microscope (FE-SEM, Zeiss Supra 35VP, Germany). The nanophase structure of PUU-POSS was observed using high resolution TEM (JEOL2100 field emission gun transmission electron microscope, FEG-TEM, Germany). The TEM samples was embedded in an aromatic acrylic resin (LR White Embedding Medium, EMS, USA), and then cryo-microtomed into a thin section using a CR-X cryosectioning system (RMC Boeckeler, Germany), and then stained by Ruthenium tetroxide (RuO_4) vapour. The porosity of the membranes was determined using gravimetry. The dimensions of the scaffold discs (16 mm in diameter and 3 mm in thickness) were cut using a cutter. Average radius and height was measured for each disc to the nearest 0.01 mm using a digital caliper. The weight of the sample was measured using a high sensitivity balance (resolution 0.01 mg). The apparent density and porosity of the scaffolds were calculated using the equation (Supplementary Information, Equation SI-1) and listed in Supplementary Table S1). A mercury intrusion porosimeter, (PoreMaster 60GT, Quantachrome, UK) was used to characterise the pore structure including the pore size, pore volume, size distribution, surface area of the freeze-dried scaffolds (Supplementary Table S2).

2.4. Cell culture, cell proliferation and immunochemical staining

Primary human dermal fibroblast (HDF) cells (Culture Collections, HDF (106-05a) UK) were cultured in Dulbecco's modified Eagles medium (DMEM) (Gibco, Life Technologies, UK), supplemented with 10% foetal bovine serum (FBS) (Gibco, Life Technologies, UK) and 1% antibiotic (50 μg/mL streptomycin, 50 μg/mL penicillin) solutions (Gibco, Life Technologies, UK), and incubated at 37.5 °C.

Polymer discs (diameter 11 mm, thickness 3 mm) were cut from the 50% cuboids fabricated from each of the three PUU-POSS scaffold conditions. Discs (n = 7) were sterilized in 70% ethanol and stirred for 30 min, followed by air drying in a sterile cell culture hood, before finally being washed four times in sterile phosphate-buffered saline (PBS). All discs were placed in 48 well Corning culture non-treatment plates (VWR International, UK) pre-incubated in 500 μl of supplemented culture media for 24 h. Cells suspensions from passage 4th (P4) at five different densities (3×10^4, 9×10^4, 27×10^4, 81×10^4, and 243×10^4 cells/cm^3; corresponding respectively to 0.85×10^4, 2.5×10^4, 7.7×10^4, 23×10^4, and 69×10^4 cells/scaffold) were then seeded onto each scaffold and cultured under standard culture conditions of 5% CO_2

in incubator at 37.5 °C with medium renewal every 2–3 days. Wells containing 11 mm Thermonax coverslips (Nunc, USA) were used as tissue culture plastic (TCP) positive controls.

The metabolic activity of cells was monitored to determine cell viability through alamarBlue® (AB) (Serotec Ltd, Kidlington, UK) testing performed according to manufacturer's instructions. One day post seeding, scaffolds were transferred to a new 48-well plate to avoid false positive readings from cells adhering to the tissue culture plastic rather than the scaffold. Readings were taken at day 1, 3, 7, 10 and 14. The absorbance of the scaffolds and control were measured by a fluorescence plate reader (Fluroskan Ascent FL reader, Thermo Labsystems, Basingstoke, UK) at 530 nm excitation wavelength and 620 nm emission wavelength. The alamarBlue™ reading in cell culture medium of TCP/polymer scaffold without cell seeded was used as a negative control. The total deoxyribonucleic acid (DNA) content quantification was determined using the fluorescent Hoechst 33258 stain and the amount of extracellular acid-soluble collagen (types I-V) was measured using the Sircol™ assay (Biocolor, UK) at each time point as day 1, 3, 7, 10 and 14.

Fibroblast cytoskeleton and attachment to the various PUU-POSS scaffolds was studied using Fluorescein Isothiocyanate Labeled (FITC)-labeled phalloidin, Alexa Fluor® 488 (Life-Technologies, UK) for F-actin and 4′,6-diamidino-2-phenylindole (DAPI) (Sigma-Aldrich, UK) for nucleic acid staining. Briefly, cell-laden polymer discs were harvested at day 3, day 7 and day 10, first fixed with 4% paraformaldehyde (PFA, Muto Pure Chemicals, Sigma, UK) for 12 h at 4 °C and rinsed three times with PBS. All stained images were taken using a confocal microscope (Leica TCS SP8vis, Germany) with ×10 and ×20 water immersion objective lens. The Z-stacking images were acquired by scanning 9-point areas (3 × 3) throughout 3 mm thickness of the scaffold at 7um/Z-step. Images stacks were visualized and analyzed using LAX X software (Leica, Germany). 3D reconstructions were compiled from 428 imaged sections (each of 7 μm thickness).

2.5. Data analysis

Statistical analysis of the results was performed using GraphPad Prism 6 (GraphPad Software San Diego, CA). Statistical significance was calculated by 2-way ANOVAs (for comparisons across more than two groups) analysis of variance (ANOVA), with Tukey multiple comparison post-hoc analysis where a value of $p < 0.05$ was considered statistically significant.

3. Results

3.1. Fabrication of hierarchical interconnected porous PUU-POSS scaffolds

The 3D-TIPS technique comprises two low-cost manufacture stages to produce a final soft PUU elastomer construct with its complex shape and hierarchical interconnected porous structure (Fig. 1). Solution-based poly(carbonate-urea)urethane (PUU) nanohybrid terminated by polyhedral oligomeric silsesquioxane (POSS) was synthesised in house [38]. Preforms were printed from water-soluble polyvinyl alcohol (PVA) by using an inexpensive fused deposition modelling (FDM) extruder. Printed preforms were injected with PUU-POSS and submerged into deionised water, resulting in confined coagulation and uniform phase separation of PUU-POSS prior to PVA dissolution, driven by diffusion water and solvent along the interconnected micro-channels (Fig. 1A). The resulting scaffold was inversely shaped internally to the PVA preform with continuous interconnection, overcoming the weak interfaces created when polymer layers are printed on each other directly. Anonymised CT scans of facial structures (nose and ear) were used to produce bespoke, patient-specific preforms and their daughter scaffolds (Fig. 1B) and evaluated by optical, micro-CT and scanning electron microscope (SEM) (Fig. 1C–1H).

PUU-POSS scaffolds demonstrated controllable and hierarchical porous structures (Fig. 1C–1H), with regularly ordered and completely interconnected pores of 300–400 μm in-plan and 100–400 μm cross-section, accommodating the inverse porous structure of the infill density and resolution of the PVA preform. A random finer porous surface structure was evident throughout the scaffold strut at a few microns to nanometre scale (Fig. 1G&1H)) resulting from uniform phase separation of PUU-POSS solution within the preform multi-micron-channels, which are significant advantages over FDM printing techniques and TIPS process alone. Macro- to microscopic modifications to scaffold porosity were easily achieved by varying coagulation condition and the printed infill density of the PVA preform (Fig. 2 and Table 1 and Table S2 in Supplementary Data).

3.2. Tuneable nanostructure and hyperelasticity of the elastomer scaffolds by 3D-TIPS

Using different phase separation temperatures, we controlled PUU-POSS scaffold hierarchical porosity and phase-structure to produce scaffolds with a wide range of mechanical properties whilst maintaining a constant external architecture. Based on Onsager's thermodynamic diffusion equation [56] and Flory-Huggins' polymer solution thermodynamics theory [57,58], different temperature processes were deigned and applied in order to control the speed of the polymer solution phase separation and dissolution of PVA in order to produce scaffolds with desired quality and properties. Three 50% infill density PUU-POSS scaffolds using differing thermal conditions were manufactured (in Table 1 and Supplementary Information SI.2). PUU-POSS coagulation and micro-phase separation were varied by controlling water and solvent diffusion rates within the micro-channels of a PVA preform and dissolution rate of PVA at different temperatures. The 50RTC +H scaffolds underwent fast coagulation (liquid–liquid phase separation) at room temperature (25 °C) following thermal annealing in water at 40 °C; the 50CC scaffolds underwent slow cryo-coagulation (liquid–solid phase separation) of frozen PUU-POSS solution (at −20 °C overnight) in ice water at 0 °C, and the 50CC +H scaffolds underwent the same process to 50CC followed by thermal annealing in water at 40 °C for 3 h.

Differential scanning calorimetry (DSC), wide-angle X-Ray diffraction (WAXD) analysis, scanning electron microscopy (SEM) and high-resolution transmission electron microscopy (HRTEM) confirmed different phase structures for the three different 50% PUU-POSS scaffold types (Fig. 2). 50RTC+H scaffolds demonstrated the glass transition temperature (*Tg*) of −30 to −35 °C on DSC (Fig. 2A), suggesting a soft amorphous rubber-phase structure throughout. WAXD analysis showed three background halo peaks centred at approximately $2\theta = 19.9°$, 31.3° and 41.3°, corresponding to a nanophase structure driven by different hydrogen bonds between hard-hard and hard-soft segment interactions at varying distances[59] (Fig. 2B). HRTEM images (Fig. 2J) also supported a quasi-random nanophase structure of soft and hard segments, with evidence of a diffusion halo from electron diffraction. It is noted that the fine, dark and dense hard nano-domains, resulting from selectively RuO4 stained urethane regions, self-assembled and interconnected through bright and continuous soft polycarbonate domains. No crystals and clusters of POSS nanocage were observed, indicating well distributed as PUU chain ends.

50CC scaffolds demonstrated a sharp melting peak appeared at 45–50 °C on DSC, with the same Tg at ~30 °C attributed to the amorphous region of the soft segment chains, as well as a smaller broad peak at 190 °C likely corresponding to the second Tg of the

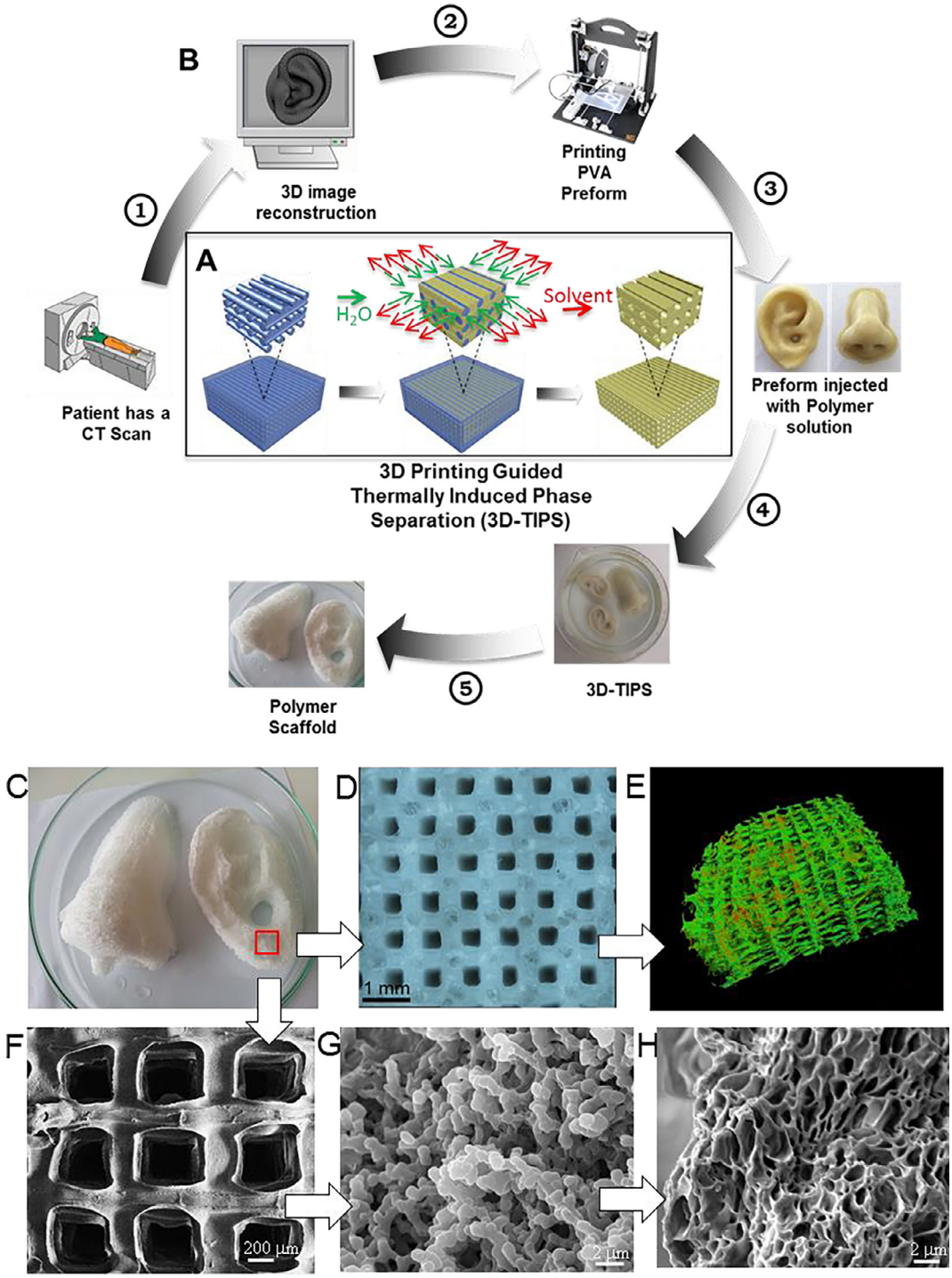

Fig. 1. Schematic outlining the multi-micro-channel-controlled phase separation of 3D PUU-POSS scaffolds with hierarchical interconnected porous structure. (A) An overall schematic showing how the 3D printed preform phase separation (3D-TIPS) technique works in relation to patient care, from CT scan to final polymer mesh implant, in order to create uniquely shaped polymer meshes to suit individual patient needs. (B) A schematic demonstration of the principle of multi-micro-channel-controlled 3D phase separation in the 3D-TIPS technique stepwise from left to right, with the preform shown in blue and the nanocomposite polymer shown in yellow. (C) Photo, (D) Optical microscopic, (E) micro-CT, (F-G) SEM images of the surface and (H) the cross section. (For interpretation of the references to colour in this figure legend, the reader is referred to the web version of this article.)

hard segment chains (Fig. 2A). On XRD analysis, two sharp Bragg diffraction peaks at $2\theta = 20.0°$ and 23.4° were superimposed onto a broad amorphous halo at $2\theta = 19.9°$ with inter-planar spacing (d-spacing) of 0.44 nm and 0.38 nm, suggesting the lateral distances in the interfaces of crystallised soft segments (Fig. 2B). HRTEM images (Fig. 2K) further supported a structure of bright polycarbonate crystalline domains with distinctly ordered lattice structures within the random nanophase structure, with an electron diffraction pattern with d-spacing 0.43 nm and 0.37 nm in agreement with XRD analysis.

In 50CC+H scaffolds, the sharp melting peaks seen in 50CC scaffolds on DSC almost disappeared following thermal treatment, with the reappearance of the clear step of *Tg* at −35 °C suggesting reversion back to a rubber phase with a small residual peak at the

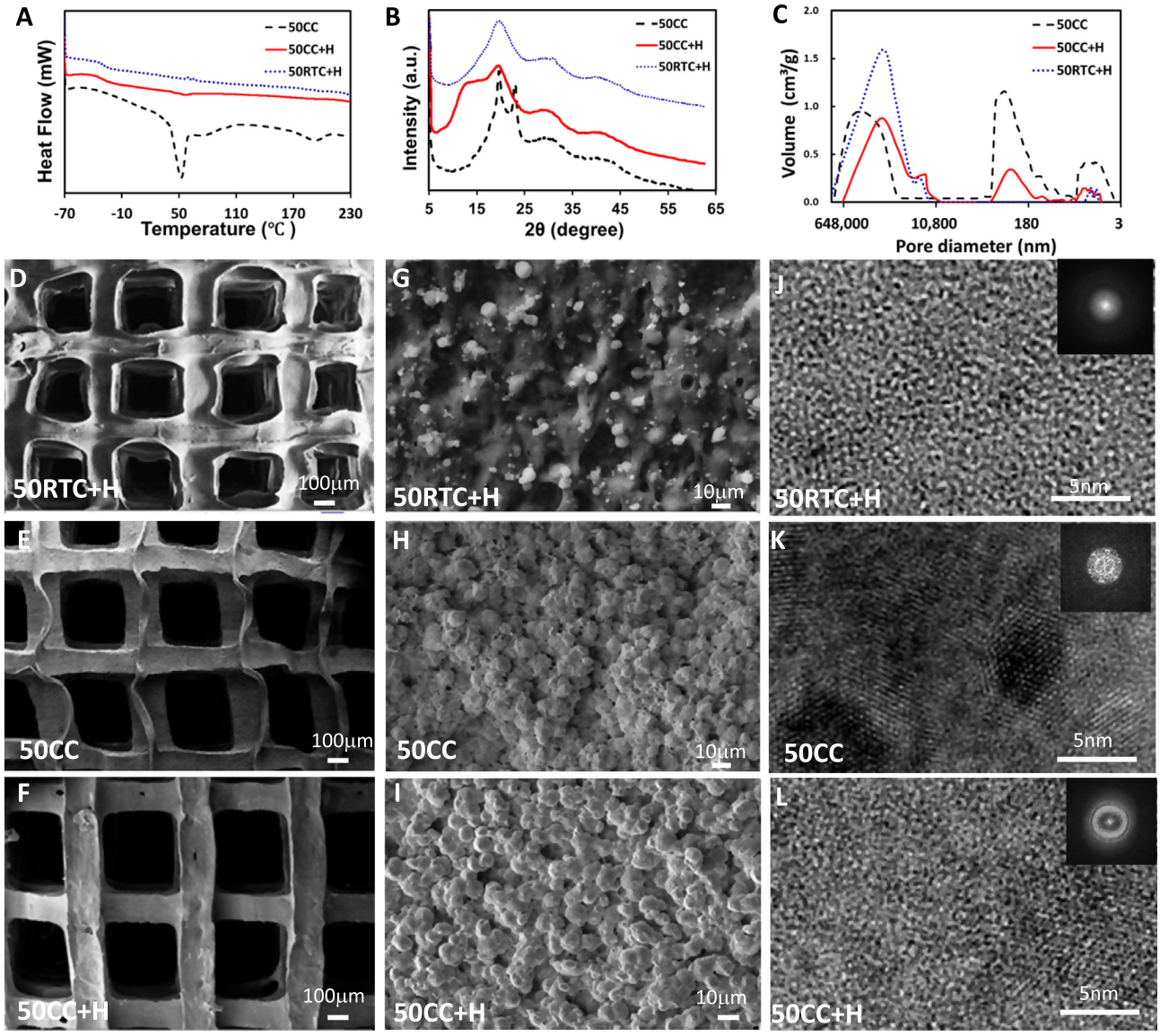

Fig. 2. Phase transitions, crystalline structure, pore size distribution, morphology and mechanical properties of 3D PUU-POSS scaffolds (50% infill density) with varying processing temperatures. (A) Differential scanning calorimetry (DSC) traces of scaffold meshes. (B) Wide-angle X-ray diffraction (WAXD) analysis of scaffold meshes. (C) Mercury porosimeter measurement of pore size and distribution. (D-I) SEM, and (J-L) HRTEM images demonstrating variations in micro-/nano-phase separation of PUU-POSS scaffolds with differing phase separation processes (the inset presents fast Fourier transform (FFT) pattern). (D, G, J) 50RTC+H, (E, H, K) 50CC, (F, I, L) 50CC+H.

melting temperature likely due to unrelaxed crystal regions from the soft segment chains (Fig. 2A). On XRD analysis, the crystal structure also almost disappeared (Fig. 2B), relaxing the long-distance order to a quasi-random amorphous structure with a similar diffraction profile to 50RTC+H comprising three broad halo peaks. HRTEM (Fig. 2L) confirmed a quasi-random nanophase structure after the thermal relaxation at 50 °C, further confirming that the crystalline peaks seen in 50CC scaffolds are from crystalline soft segment domains.

The scaffolds are lightweight with porosity between 95 and 98% and density between 27 and 56 Kg/m^3 depending on the infilled density and processing temperature (Table S1). Obviously, the scaffold density decreased, and the porosity increased as increasing the infill density. With the same infilled density, CC group have the lowest density and highest porosity, and CC+H group in opposite. Further measurement of the pore size and distribution of the scaffold with 50% infill density by mercury porosimetry revealed the insight difference (Fig. 2C, Table S2). 50RTC+H scaffolds had a wide distribution of pore sizes, with 95.2% relative pore volume provided by a one predominates broad peak with pore diameter from 400 to 10 μm and the rest 4.84% compromising of small pore diameters ranging from 10 μm to 3 nm (Fig. 2C, Table S2), whilst SEM showed an irregular surface with a minimal number of open nano-pores (Fig. 2D and 2G). This may be due to faster diffusion and phase separation occurring at room temperature and shrinkage during post thermal treatment, resulting in the formation of a skin with fewer pores. Contrastingly, the 50CC scaffolds showed greater hierarchy in its porous structure, with distinct three peaks ranging from 400 to 10 μm, 10 μm to 100 nm and 100 to 3 nm, sharing 58.5, 22.1 and 19.4% relative pore volume and contributing to 2.7, 83.2 and 14.2% surface area (Fig. 2C, Table S2). SEM demonstrated a bead-like network of pores with diameters ranging from a few microns to nanometres stacked on top of each other (Fig. 2H and 2I), which is likely due to spherulite formation during the cryo-process. 50CC+H scaffolds had a similar bead-stacking morphology and pore size distribution, with fewer pores at

10 μm–3 nm, owing to shrinkage during post thermal treatment (Fig. 2I). It is noticed that the porosity of scaffolds of 50% infill density (only one test) calculated from the pore volume in Table S2 is slightly higher than that measured by gravimetry in Table S1, which may be attributed to different accuracy of test methods. The effects of soft elastomer and mismatch of pore structure model in mercury porosimetric measurement and analysis should be taken into account.

Through tuneable phase and porous structures, the three scaffold groups with various infill density of the PUU-POSS scaffold possessed distinct mechanical properties, supporting a capacity of 3D-TIPS technique to manufacture a range of tissue-engineering scaffolds (Fig. 3 and Table S1). Despite of highly porous structure with the porosity between 95 and 98%, the scaffolds show ductile mechanical behaviour with high fracture strain from over 50% to 300% under tensile stress. Tensile modulus (E) was the highest for each group in the 80% infill density (Fig. 3D), measuring 4.4 ± 0.6 MPa in the CC, 1.0 ± 0.1 MPa in the CC+H and 0.7 ± 0.1 MPa in the RTC+H groups, with a stepwise decrease in modulus with increasing infill density across all three groups. The modulus in the CC group was significantly higher than the lowest in RTC+H group, with the RTC+H group measuring lowest for each infill density. The 3D ordered crystalline structure in the CC group contributed to high modulus (×15 times higher than the lowest in 30% RTC+H), with these properties lost in the CC+H group once crystalline structure was relaxed through thermal treatment. However, the other tensile mechanical properties of the 80% CC infill density scaffold including ultimate strength, stain and toughness appeared underperformance, which may be attributed to less entanglements of chain during the freezing process and the poor uniformity of microporous structure generated during coagulation in the presence of less water channels.

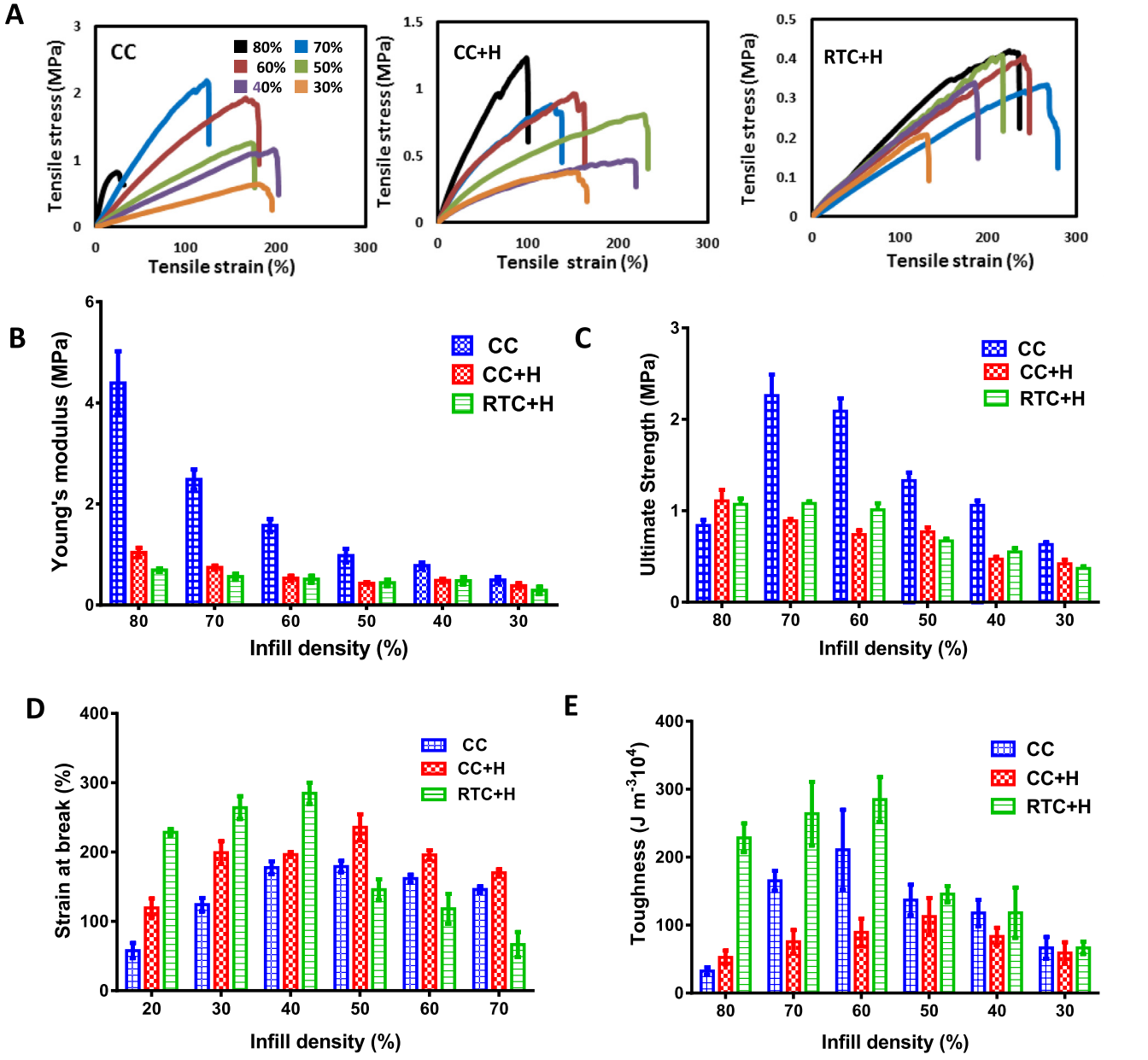

Fig. 3. Tensile mechanical properties of 3D PUU-POSS scaffolds with varying infill density and processing temperatures. (A-C) Typical tensile stress–strain profiles of three groups of the scaffolds, CC, CC+H and RTC+H with varying infill density. (D) and Tensile modulus. (E). Ultimate tensile strength. (F) Strain at break. (G) Tensile toughness of the scaffolds with increasing infill density.

Ultimate tensile strength (UTS) for scaffolds (Fig. 3B) was greatest for the CC group in the 70% infill density preforms, at 2.3 ± 0.2 MPa. For each group, there was a stepwise decline following peak UTS with increasing infill density except for 80% CC due to an increase of the non-uniformity of the scaffolds at low infill density. At each infill density, UTS for the CC group was significantly higher than the CC+H and RTC+H groups. Strain at break peaked at different infill density for each group, with the highest in the 60% RTC+H group at 285 ± 15% and the 50% infill densities of the CC and CC+H groups, at 180 ± 8% and 236 ± 19% respectively. It is also noticed that the strain at break of the RTC+H group at low infill density (up to 60%) was significantly higher (Fig. 3C) compared to the CC and CC+H groups, owning to the formation of dense skin in RTC+H group due to fast phase separation at the interface at the RT. However thermal treatment also substantially improved the ultimate strain of the CC group and outperform the other groups at the high infill density which may be contributed by dense packing between the chains after heating, in evidence of a shrinkage of 50CC+H group with a negative volume swelling ratio, −18.0%, compared to 50CC, −0.9%, Table S3. Tensile toughness (Fig. 3D) demonstrated some similar trend, with the RTC+H group exhibiting higher toughness than the CC or CC+H groups due to its lower porosity and dense skin. Toughness was the highest in the 60% RTC+H scaffold at 285 ± 33 J m^{-3} 10^4, higher than the maximum in the 60% CC group, at 211 ± 59 J m^{-3} 10^4 and 50% CC+H at 113 ± 27 J m^{-3} 10^4. This superior hyper-elasticity in the scaffolds was due to the continuous soft rubbery phase reinforced by a unique hard segment nanostructure.

3.3. Thermo-responsive stiffness memory at body temperature

Different from PUs with shape-memory property which changed a temporal shape dramatically at a transition temperature [60,61], the scaffold underwent stiffness relaxation with a limited volume change at a swelling ratio varying from −3.3 vol% to 20.6 vol% (Fig. 4 and Table S3) when incubated in standard cell culture conditions for 28 days. The level of the stiffness changes depended on the initial 3D-TIPS. Rigid 50CC scaffolds gradually softened at 37.5 °C and stabilised over 3 weeks with around 50% reduction in both *E* and UTS, whilst 50CC+H showed a slight relaxation in *E* with few changes in other mechanical properties and soft 50RTC+H scaffolds remained stable with no obvious changes (Fig. 4A and 4B). Despite this, scaffold toughness was not significantly altered due to compensation from an increase in fracture strain (Fig. 4C and 4D). This stiffness relaxation was also evident on dynamic tensile mechanical testing in over 1×10^6 cycles (Fig. 4E-4G, Table 2, and Fig. S2). 50CC scaffolds demonstrated slow stress damping and reduction of hysteresis loop areas with increasing cyclic number at constant 40% strain in response to the transition from semi-crystalline to quasi-random nanostructured rubbery structures at body temperature. In contrast, the soft rubbery 50RTC+H scaffolds displayed linear hyperelasticity under much lower cyclic stresses with almost full recovery of their original forms on load removal. 50CC+H scaffolds also showed recoverable nearly-linear stress–strain characteristics, with only a trace of hysteresis loop indicating residual inelastic energy after thermal treatment. After one million cycles, three types of scaffolds all reached to similar reversible linear hyperelasticity.

Temperature-dependent dynamic mechanical analysis (DMA) and wide-angle X-ray diffraction spectra at 37.5 °C scaffolds elucidated the association of unique phase transitions and viscoelasticity with the observed stiffness relaxation (Fig. 4H-4J and Table 2). Unlike 50RTC+H and 50CC+H scaffolds, where DMA showed typical profiles of storage modulus (E') and loss moduli (E'') as functions of temperature corresponding to the glass transition at −35 °C and rubbery plateau above room temperature, the storage modulus of 50CC scaffolds underwent a continuous decline over a wide range of temperatures above the glass transition. Furthermore, the abrupt peak in E'' previously seen around the melting point at 45∼50 °C on DSC was replaced with an unusual wide tanδ "plateau" (Fig. 4H). The prolonged viscoelastic behaviour observed in 50CC scaffolds implies a wide spectrum of relaxation times of chain segments in different length involved in the phase transition of crystal-to-amorphous rubber of the soft segments and local reorganisation of soft and hard segments. These sequential transitions from crystalline to random to quasi-random structures is proven through the disappearance of two sharp Bragg diffraction peaks at 2θ = 20.0° and 23.4° in 50CC scaffolds early in incubation and a subsequent upshifting of two amorphous halo peaks centred at 17.9° and 21.3° to three with closer packing at 19.9°, 31.3° and 41.3° over 4 weeks (Fig. 4K and 4L). Regardless of the different initial stiffness of scaffold groups, all three scaffold types eventually "remembered" to self-organise back to a thermal dynamically stable rubber phase with a unique quasi-nanophase structure, demonstrating a delicate balance between entropic and energetic contributions as seen in Fig. 2J and Fig. 4K-4M. This inverse assembling process did not cause unacceptable shape changes after 4 weeks, which we attribute to the low crystallinity and local interactions of hydrogen bonds.

3.4. Effect of stiffness memory of the scaffolds on HDF cell proliferation in vitro

Due to distinct differences of the surface and porous structure between the 3D printed scaffolds and standard 2D cell culture, it is imperative to optimize the cell seeding density on the 3D scaffolds. The metabolic activity of primary human dermal fibroblast (HDF) cells with five different densities seeded onto the 50CC scaffolds were tested over time for 10 days (Fig. 5A). Cell metabolic activity measured by alamarBlue® assay showed that one day after seeding with the same density, 3×10^4 cells/cm^3, there are significantly fewer cells attached to the 50CC scaffolds compared to standard 2D TCP control. Many cells fell or migrated to adhere to the bottom tissue culture plastic because of a large surface area and many regular micro-pores (200–400 μm) of the 3D scaffolds compared to 2D TCP. There is a small increase of cell metabolism until day 7 and then slightly increased by day 14. By increasing 3 times the cell density, 9×10^4 cells/cm^3, the cell attachment in day 1 was improved and metabolic activity of the cell increased over 14 days, following the similar linear profile as that of TCP. By further increasing the cell density to 2.7×10^5 cells/cm^3, the cell attachment at day 1 was significantly increased and the metabolic activity of the cells increased up to day 5 and then reached a plateau at cell confluence. The alamarBlue® reading for the scaffolds with the two highest seeding densities, 8.1×10^5 cells/cm^3 and 2.43×10^6 cells/cm^3, show a similar trend. The highest cell density rendered the highest cell attachment on the scaffolds, but the early cell confluence and an overall decrease in cellular activity after day 3 suggested that the cells either stopped to grow or cell metabolism decreased after confluence. Based on these results, an optimized cell density of 9×10^4 cells/cm^3 in 500 μl of cell culture medium (2.5×10^4 cells/scaffold) was then used for further experiments.

Using optimised cell seeding densities, cellular metabolic activity on the elastomer scaffolds with three different processing conditions were measured over time. The metabolic activity of seeded HDF cells increased over time on the elastomer scaffolds with different stiffness (Fig. 5B). 50CC scaffolds showed superior cell proliferation at all time points compared to 50CC+H and 50RTC+H groups, with significance at days 10 ($p < 0.001$), unlike control cells seeded on 2D – tissue culture plastic (TCP) where metabolic activity levelled off after day 10, probably due to limited surface area

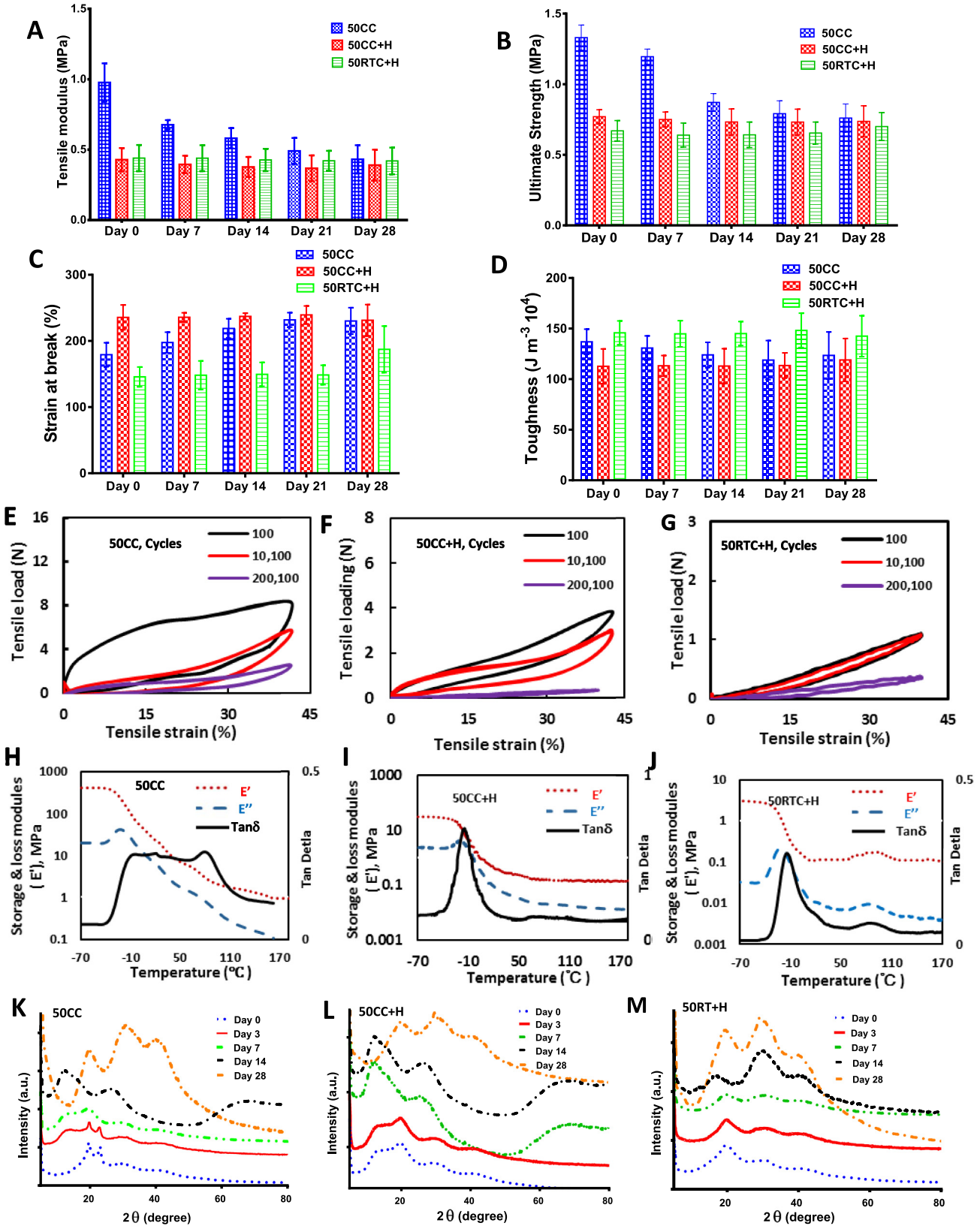

Fig. 4. Stiffness relaxation and corresponding changes of phase structure of 3D PUU nanohybrid scaffolds (50% infilled density) with different 3D-TIPS processing conditions after incubation at 37.5 °C for up to 28 days. (A) Tensile modulus. (B) Ultimate tensile strength. (C) Facture strain. (D) Tensile toughness of the scaffolds on different days of incubation (n = 6). (E-G) Dynamic tensile load (2×10^6 cycles) in strain domain and time domain. (n = 2). (H-J) Dynamic mechanical properties as function of temperature at frequency of 1 Hz. (K-M) Wide-angle X-Ray diffraction (WAXD) spectra of the scaffolds on the different days of incubation.

Table 2
Hysteresis values (i.e. energy loss) of the various scaffolds at 0–100 cycles, 10,000–10,100 cycles, and 200,000–200,100 cycles.

Hysteresis energy (J/m^3)	50CC	50CC+H	50RTC+H
0–100 cycles	160 (±11)	21 (±8)	15 (±7)
10,000–10,100 cycles	24 (±8)	14 (±3)	13 (±4)
200,000–200,100 cycles	15 (±5)	8 (±3)	11 (±4)

after confluence. Proliferation and migration, as measured by increasing DNA concentrations in HDF cells and deposition of extracellular acid-soluble collagen (types I – V) by HDF cells cultured on 3D scaffolds with time, showed that the 50CC scaffold resulted in the highest values at all time points respectively (Fig. 5C and 5D). Live/dead staining corroborated this increase in proliferation with live HDF cell attachment observed within the 3D interconnected structure of the scaffolds (Fig. 6). Cells were observed migrating toward the inner digital porous network of 50CC scaffolds from day 3 (Fig. 6A-A2), covering more than half of the scanned area by day 7 (Fig. 6B-B2). By day 10, live cells were visualised throughout the scaffolds' interior, filling the large infill generated pores (Fig. 6C-C2).

Confocal microscopy with counterstaining, SEM imaging illustrating cell morphology and histological analysis of fixed cell-scaffold specimens provided further evidence of HDF proliferation, self-organisation and HDF cells-scaffold interactions during the stiffness relaxation. On immunofluorescence with HDFs stained green for actin and blue for nuclei, cell penetration and attachment were clearly seen in all three PUU-POSS scaffold groups at days 3 and 7 (Fig. 7). Cells self-organised within the scaffold pores at different depths (showing different colors), confirming cell penetration through to the scaffold construct core (Fig. 7E, E1), and well-orientated blue and green interference fringes (Fig. 7D-D2 and 7E-E2) and circular patterns (Fig. 7D-D2) suggested alignment and self-organisation preferences at different local layers throughout the scaffold. 3D-reconstructed confocal images (Fig. 7A3-F3) corroborated the 50CC scaffolds' superior cell attachment and penetration, intra-scaffold proliferation and cellular organisation throughout the period of stiffness relaxation compared to 50CC +H and 50RTC+H (Fig. 5A2-C2). Histological staining of a lateral cross section of the fixed cell-scaffold complexes on day 10 confirmed cell attachment and proliferation to the inside of all scaffold groups, with cells aggregating around the open infill pore edges created through 3D printing (Fig. 8A-8F). HDF morphology on the surface across the scaffold groups was showed using SEM (Fig. 8-G-8L), with flatter cell bodies and long actin spindles on day 3 of the early proliferation and with increased cell coverage on the surface of all three scaffolds on day 7 (highlighted in blue). It is of note that the high density of cell proliferation was visualised on the scaffolds from the 3D reconstructed fluorescent images (Figs. 6 and 7), which was compiled from 428 images scanned throughout 3 mm thickness of the scaffold at 7um/Z-step (as described in Section 2.4). The H&E stained cell clusters within the thin layer of cross section (4 μm in thickness) of the scaffold (Fig. 8A-F) and the SEM morphology of the cells on the top surface of the scaffold (Fig. 8G-L) provided supporting evidence, in consistence with the results of the cell migration and proliferation throughout the scaffolds by 3D confocal microscopy.

There was a clear association of the 50CC scaffolds' stiffness relaxation and porous surface topography with cell adhesion and metabolic activity compared to the other 'softer' 50CC+H and 50RTC+H processing conditions. Unlike 50RTC+H scaffolds, it is hypothesized that the high porosity and hierarchical porous structure in the 50CC scaffolds (Table S1 and S2) allowed fast diffusion of nutrients and oxygen from the cell culture media to the cells, whilst its high initial stiffness and sequential stiffness relaxation may have further accelerated cellular attachment, metabolic activity and proliferation in comparison to the softer 50CC+H scaffolds.

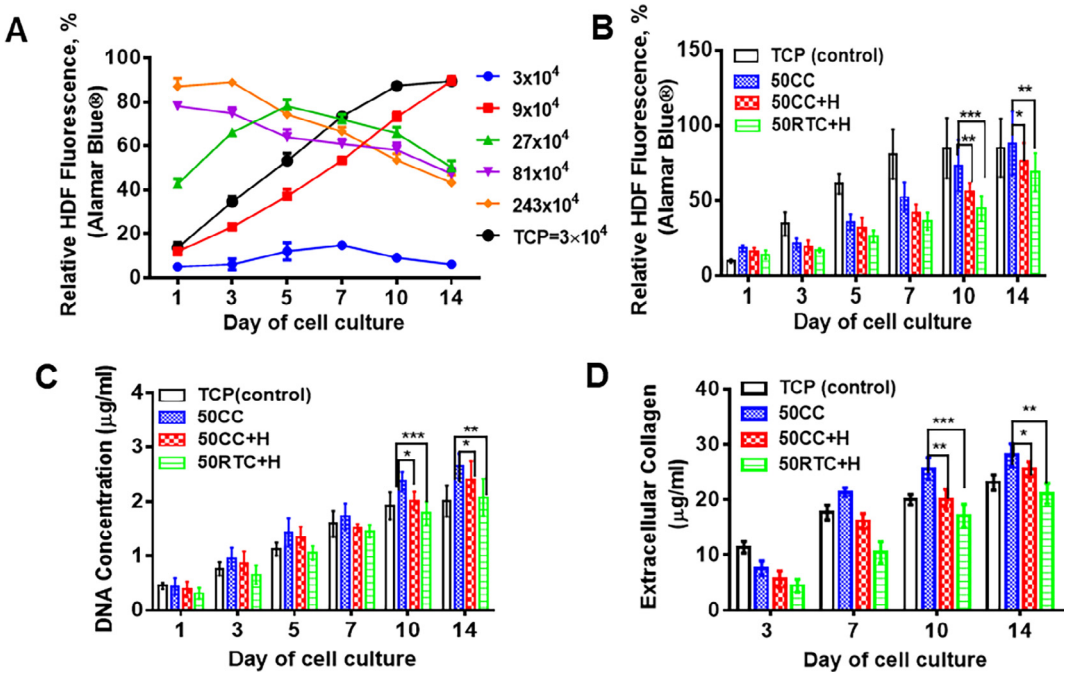

Fig. 5. Cell seeding density test and cellular proliferation of human dermal fibroblasts (HDF) on PUU-POSS scaffolds. (A) Metabolic activity of HDF on PUU-POSS scaffolds. 50CC, and the collagen coated tissue culture plastic (TCP) control using different seeding density over 14 days, measured by the alamarBlue™ fluorescence assay. TCP seeding density is 3×10^4 cells/cm^3. (B-D) HDF cell proliferation on scaffolds subjected to different phase separation conditions measured by (B) the alamarBlue® fluorescence assay and (C) total DNA analysis. (D) Extracellular acid-soluble collagen (types I-V). $^{*}p < 0.05$, $^{**}p < 0.01$, $^{***}p < 0.001$, $^{****}p < 0.0001$, errors bar = SD ($n = 5$, scaffolds in each group at each time-point).

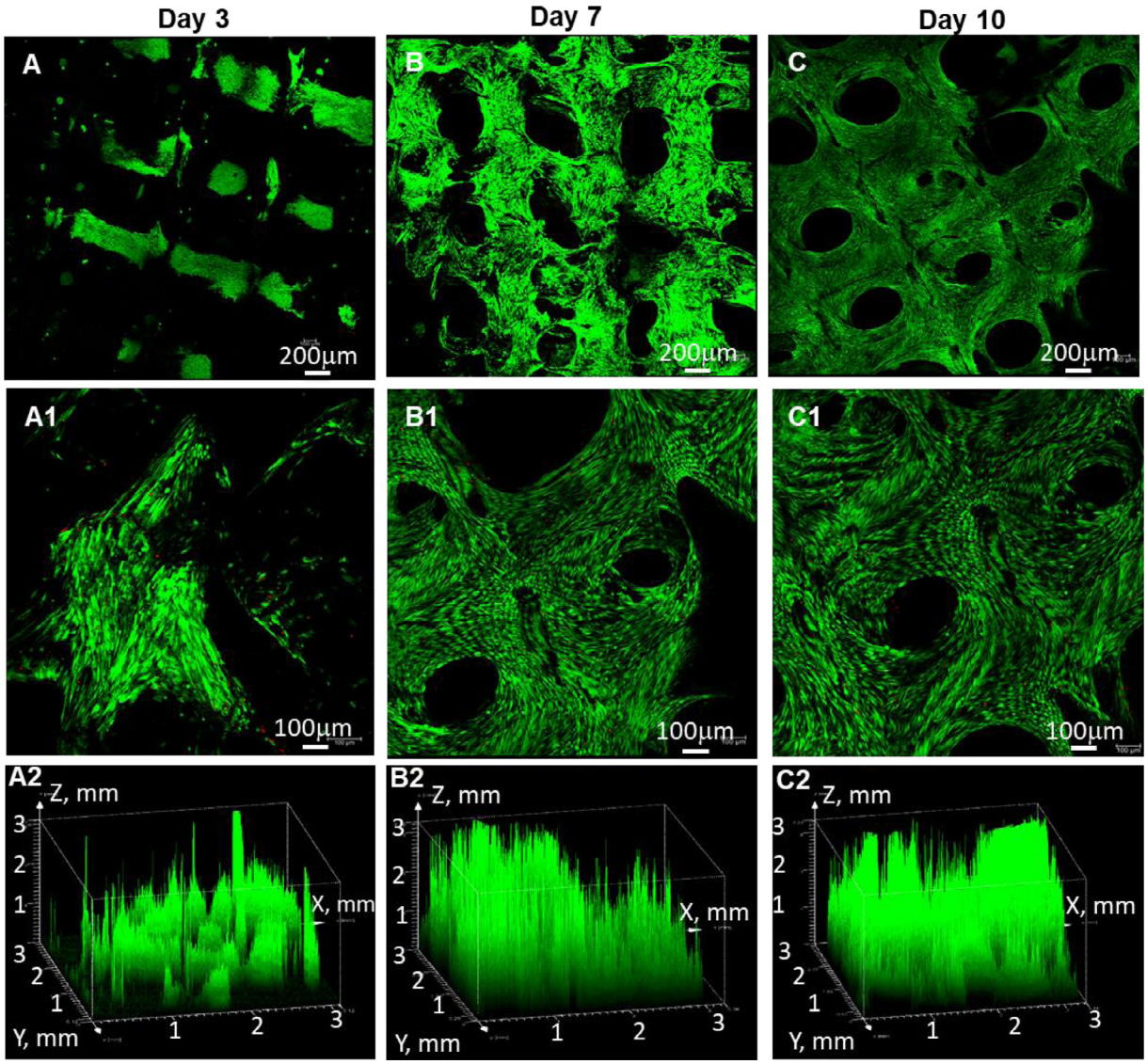

Fig. 6. Live-dead staining confocal microscopy of cellular proliferation of human dermal fibroblasts on PUU-POSS scaffolds, 50CC by live-dead staining confocal microscopy. (A-C) (×10 objective lens) and (A1-C1) (×20 objective lens) HDF proliferation on 50CC scaffolds at day 3, day 7 and day10. (A2-C2) 3D reconstructions of fluorescent light intensity by confocal microscopy (×10 objective lens).

4. Discussion

We have demonstrated the manufacture of a body-temperature-responsive bespoke tissue scaffold through a reliable, versatile and cost-effective 3D-TIPS indirect printing technique. Large and complex 3D scaffolds with a wide range of structures and properties were fabricated from PUU-POSS nanohybrid elastomer solution confined within a scalable 3D-printed interconnected PVA preform network, with dual control of multi-level phase-separation and polymer crystallinity. Thermal control of PUU solution coagulation and micro-phase separation of polymer chains within the preform network micro-channels produced 3D scaffolds with identical and uniform macroscopic dimensions and polymer content but with highly variable micro-/nano-structures, biomechanical and cellular properties. Scaffolds (CC group) subjected to temperatures below freezing during fabrication developed semi-crystalline structures, more nano-pores and less shrinkage, rendering them stronger and stiffer. Scaffolds (RTC+H group) processed at room temperature were softer and hyperelastic with higher strain and toughness values, due to the formation of quasi-random nanophase structures with packed hard domains acting as physical crosslinking points within the continuous amorphous rubber. Digital control of PUU-POSS scaffold infill density from 80 to 30% can also be manipulated to further widen the range of scaffold specification options without altering chemistry or using crosslinking, allowing specifications of each to best match the properties of various native tissues.

The most intriguing property of these scaffolds, that of 'stiffness memory', is driven by the reverse self-assembly of phase transition of 3D ordered crystalline structure into quasi-random nanostructures of soft and hard segments at body temperature, which imparts the unique and desirable dynamic mechanical properties of stiffness relaxation with unnoticeable shape change. The small volume changes, due to the relaxation of ordered chain packing at the melting point of soft segments within the uniform interconnected porous network, contribute to the stability of the scaffold shape with little deformation. This is different from the shape memory of polymers with a large strain (entropic elasticity) involved in the initial temporal shape. Regardless the initial stiffness generated at different thermal process conditions, 3D-TIPS PUU-POSS scaffolds 'remembered' to relax to its intrinsic hyperelastic rubber phase around the melting temperature of the soft

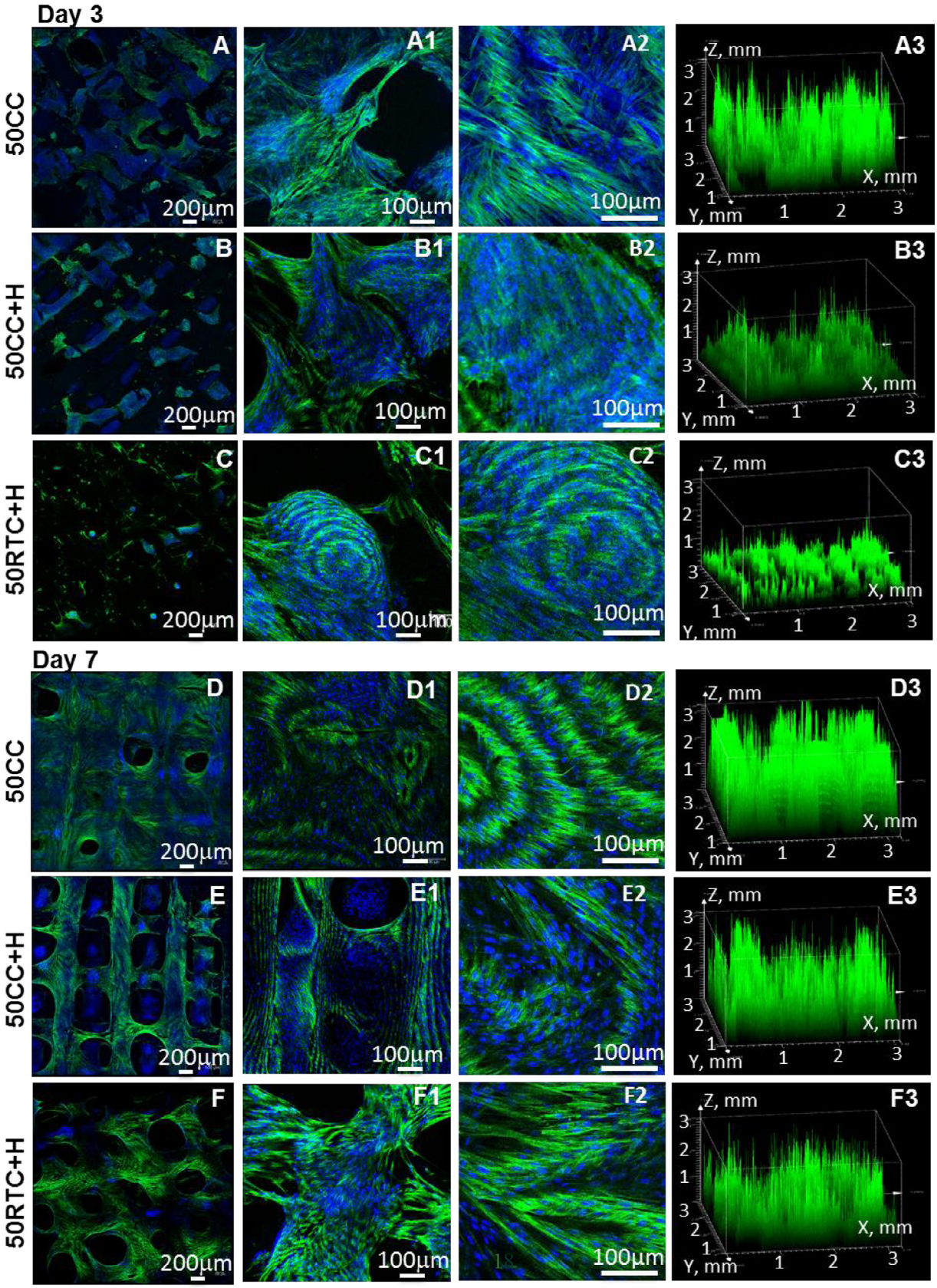

Fig 7. HDF cell proliferation on PUU-POSS scaffolds at difference stiffness relaxation stages. Confocal microscopy images showing stained HDF actin fibers (green) with counterstained (blue) nuclei at (A-C) day 3 and (D-F) day 7; (A-F) ×10 objective lens; (A1-F1) ×20 objective lens; (A2-F2) close-up images from A1-F1 (∼×45 objective lens); (A3-F3) 3D reconstructions of fluorescent light intensity by confocal microscopy (×10 objective lens).

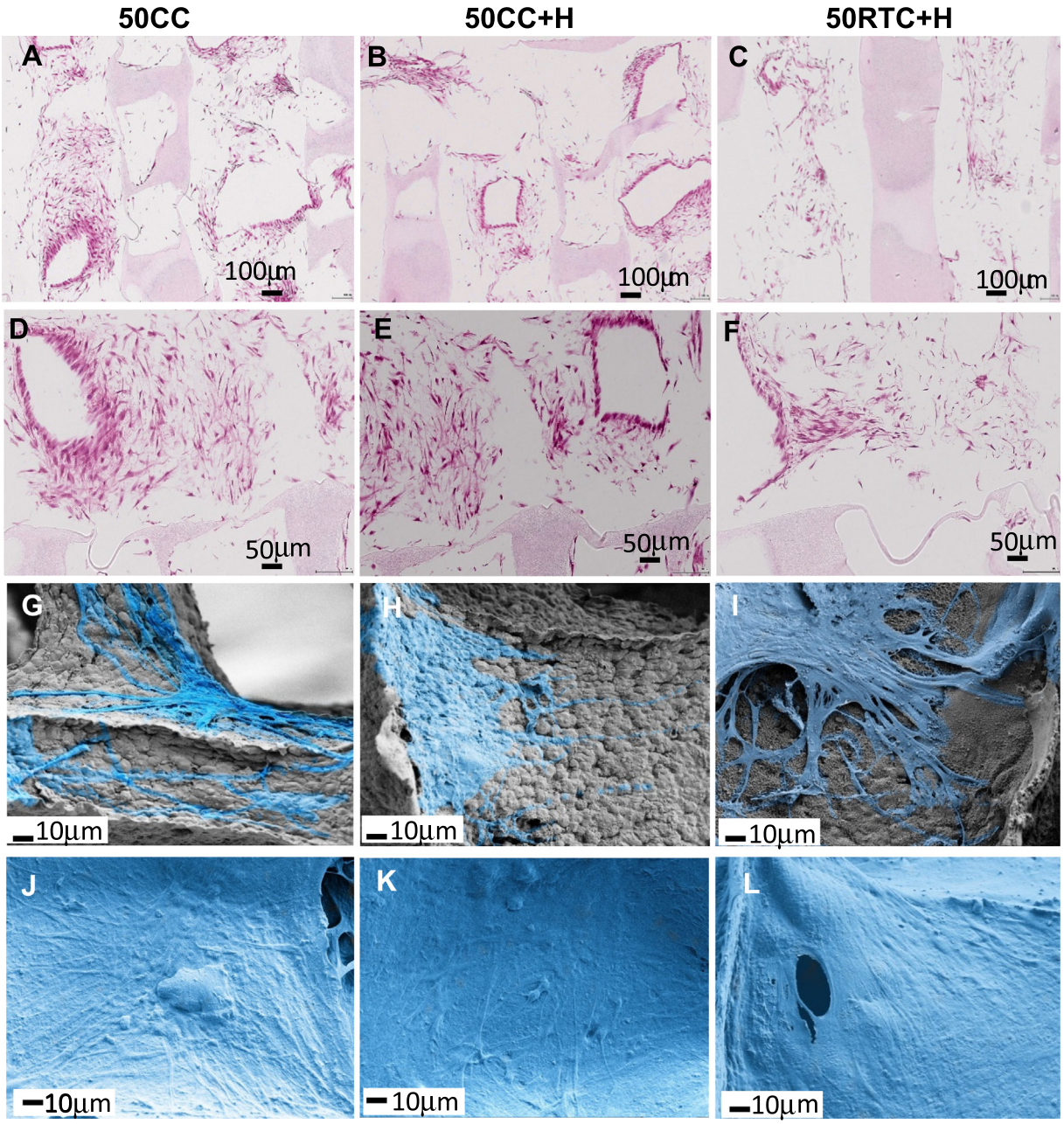

Fig. 8. Histological and scanning electron microscopic analysis of HDF cells on PUU-POSS scaffolds at different stage of stiffness relaxation. (A-C) Fixed sections showing HDF cell proliferation around the scaffold pores in plane at day 10, stained with H&E (×10 objective lens). (D-F) are close-up images from (A-C) (~×20 objective lens). (G-L) SEM images showing HDF cell attachment and morphology at day 3 (G-I) and day 7 (J-L). (A, D, G, J) 50CC; (B, E, H, K) 50CC+H; (C, F, I, L) 50RTC+H.

segments. Although the scaffolds could not re-crystallise from the solution after 3D-TIPS process, the tendency of re-crystallisation or densely packing of PUU-POSS soft segments from the rubber phase at a suitable temperature, below the Tm (42 °C) and above Tg (−30 to −34 °C), may still be thermodynamically favourable. Therefore, such 'stiffness memory' may be theoretically reversible or partially reversible despite the fact that it is kinetically slow.

The semi-crystalline rigid PUU-POSS constructs, coupled with stiffness relaxation and 3D-interconnected nano-pores produced in our study, resulted in the greatest HDF cells-scaffold attachment, penetration, migration and proliferation throughout these rigid scaffolds. Scaffold elasticity and viscoelasticity were revealed strong influences in various types of cell behaviour in well-established 2D models of variable stiffness polymers [55]. However, the stiffness changes in those 2D models were often coupled with the change of molecular structure due to the use of crosslinking agents. This study reveals for the first time that strong HDF cells proliferation remains during scaffold stiffness relaxation without changes in matrix molecular structure.

Like native ECM, these 3D scaffolds appear to offer a complex structure that is organised at several magnification scales. The scaffold shape and digitally controlled large pores (100–400 μm) provided specific guides and boundaries for HDF cells growth, offering the framework for local cells adhesion and proliferation. The cells demonstrated permeation into scaffolds, penetrating through the 3D digitally printed interconnected pores. The disordered, rough and nano-porous surface topography created by phase separation, may have contributed to improving cell adhesion and metabolic activity. The high continuous surface area within the scaffolds of 50CC (58.5 m^2/g) and 50CC+H (24.5 m^2/g, Table S2)

allowed fast diffusion of nutrients from the cell culture media to the cells. The *in vitro* study suggests that the level of porosity (50% infill density) and size of the pores (100–400 μm) of the scaffolds are adequate to facilitate the attachment, migration and proliferation of HDF cells on the 3D-TIPS scaffolds.

As aforementioned, despite several reports on manufacturing polymeric scaffold by combination of 3D printing and TIPS [53,54], dual-level regulation of porosity and stiffness relaxation, using design to control macro-to-micro scale changes and thermally controlled phase-separation to govern micro- to nano-scale structure and properties, has not been described. The technique allows use of a wide range of biofunctional and unprintable polymers and their composites, and permits flexibility in the architecture of fabricated constructs, tunability not presently achievable through current direct printing techniques or phase-separation alone. New and existing polymer solutions, especially high molecular weight, and their nanocomposite solutions can be directly shaped into intricate and bespoke patient-specific 3D scaffolds through a one-stop processing technique. This low-cost method with short-lead time shows capability of shaping these highly permeable and lightweight 3D constructs, from a variety of unprintable degradable, non-degradable polymers and nanocomposite. This is especially the case for expensive new biomaterials with a low quantity, as well as the biomaterials that have been extensively studied at various preclinical, clinical and proven stages.

Controllable scalability of our technique produced an array of constructs from the same polymer solution, without altering chemistry or using crosslinking, allowing specifications of each to best match the properties of various native tissues. The responses of various types of cell-lines to these tuneable scaffolds are currently under investigation with positive results, including human bone-marrow derived mesenchymal stem cells, human bronchial epithelial cells, human lung fibroblast, mouse embryonic dermal fibroblasts, which will be featured in future publications. This is a potentially highly desirable property for aiding biological tissue remodelling following surgical tissue reconstruction. The improved cell viability on the 3D-TIPS scaffolds represents a promising technique platform for the development of implants and scaffolds in various tissue engineering disciplines, with matched structures and mechanical properties to suit cell-lines, tissues and organs.

5. Conclusion

3D-TIPS technique opens up the use of a wide range of biofunctional and previously unprintable polymers and their nanocomposites and permits tunability in the architecture and stiffness of fabricated constructs not previously achievable via direct printing techniques or phase-separation alone. The method is low-cost with a short-lead time, even for intricate and bespoke patient-specific implants. The potential for improved cell growth and bioresponsiveness of scaffolds in the postoperative healing period, due to stiffness relaxation, represents a promising technique platform for the development of biological responsive tissue-engineered implants, devices and surgical robotics, with matched dynamic mechanical properties to suit dynamic cell-lines, tissues and organs.

Competing financial interests

The authors declare no competing financial interests.

Acknowledgments

This work was supported by the UK Engineering and Physical Sciences Research Council (EPSRC EP/L020904/1, EP/M026884/1 and EP/R02961X/1). We would like to thank all colleagues who helped and support this project including Samar Hamad and Stephanie Bogan, Yutong Li, Leila Nayyer and Wai Ho at UCL for technical support of cell culture and characterisations. Dr Hang Song and Abdul Ghani (Brunel) for DSC and XRD scans, Dr Christopher Thrasivoulou, Daniel Ciantar and Tim Robson (UCL) for confocal imaging technical support, Angela Richard-Londt, Francesca Launchbury and Jessica Broni (UCL IQPATH) for histological services.

Appendix A. Supplementary data

Supplementary data to this article can be found online at https://doi.org/10.1016/j.actbio.2018.09.016.

References

[1] P. Ciarletta, M. Destrade, A.L. Gower, On residual stresses and homeostasis: an elastic theory of functional adaptation in living matter, Sci. Rep. 6 (2016) 24390.
[2] N.A. Kurniawan, C.V.C. Bouten, Mechanobiology of the cell–matrix interplay: catching a glimpse of complexity via minimalistic models, Extreme Mech. Lett. 20 (2018) 59–64.
[3] M.F. Griffin, Y. Premakumar, A.M. Seifalian, M. Szarko, P.E.M. Butler, Biomechanical characterisation of the human nasal cartilages; implications for tissue engineering, J. Mater. Sci.-Mater. Med. 44 (12) (2016) 3460–3467.
[4] E.C. Ekwueme, B. Choi, C.F. Yu, R. Rao, M. Pellegrini, M. Mohiuddin, J.W. Freeman, Sub-failure stretch injury response in rat Achilles tendon, Regener. Eng. Transl. Med. 3 (4) (2017) 239–246.
[5] O. Chaudhuri, S.T. Koshy, C.B.D. Cunha, J.W. Shin, C.S. Verbeke, K.H. Allison, D.J. Mooney, Extracellular matrix stiffness and composition jointly regulate the induction of malignant phenotypes in mammary epithelium, Nat. Mater. 13 (10) (2014) 970–978.
[6] F. Broders-Bondon, T.H. Nguyen Ho-Bouldoires, M.E. Fernandez-Sanchez, E. Farge, Mechanotransduction in tumor progression: the dark side of the force, J. Cell Biol. 217 (5) (2018) 1571–1587.
[7] Z. Razinia, P. Castagnino, T. Xu, A. Vázquezsalgado, E. Puré, R.K. Assoian, Stiffness-dependent motility and proliferation uncoupled by deletion of CD44, Sci. Rep. 7 (1) (2017) 16499.
[8] W.D. Merryman, I. Youn, H.D. Lukoff, P.M. Krueger, F. Guilak, R.A. Hopkins, M.S. Sacks, Correlation between heart valve interstitial cell stiffness and transvalvular pressure: implications for collagen biosynthesis, Am. J. Physiol.-Heart Circul. Physiol. 290 (1) (2006) H224–H231.
[9] D. Joaquin, M. Grigola, G. Kwon, C. Blasius, Y. Han, D. Perlitz, J. Jiang, Y. Ziegler, A. Nardulli, K.J. Hsia, Cell migration and organization in three-dimensional in vitro culture driven by stiffness gradient, Biotechnol. Bioeng. 113 (11) (2016) 2496–2506.
[10] E.H. Barriga, K. Franze, G. Charras, R. Mayor, Tissue stiffening coordinates morphogenesis by triggering collective cell migration in vivo, Nature 554 (7693) (2018) 523–527.
[11] C.D. Hartman, B.C. Isenberg, S.G. Chua, J.Y. Wong, Extracellular matrix type modulates cell migration on mechanical gradients, Exp. Cell Res. 359 (2) (2017) 361–366.
[12] A. Pathak, S. Kumar, Independent regulation of tumor cell migration by matrix stiffness and confinement, PNAS 109 (26) (2012) 10334–10339.
[13] F.N. Kenny, Z. Drymoussi, R. Delainesmith, A.P. Kao, A.C. Laly, M.M. Knight, M.P. Philpott, J.T. Connelly, Tissue stiffening promotes keratinocyte proliferation via activation of epidermal growth factor signaling, J. Cell Sci. 131 (10) (2018) x.
[14] M.E. Piroli, E. Jabbarzadeh, Matrix stiffness modulates mesenchymal stem cell sensitivity to geometric asymmetry signals, Ann. Biomed. Eng. (2018) 1–11.
[15] K. Ye, X. Wang, L. Cao, S. Li, Z. Li, L. Yu, J. Ding, Matrix stiffness and nanoscale spatial organization of cell-adhesive ligands direct stem cell fate, Nano Lett. 15 (7) (2015) 4720.
[16] N.X. Liu, M. Zhou, Q. Zhang, T. Zhang, T.R. Tian, Q.Q. Ma, C.Y. Xue, S.Y. Lin, X.X. Cai, Stiffness regulates the proliferation and osteogenic/odontogenic differentiation of human dental pulp stem cells via the WNT signalling pathway, Cell Prolif. 51 (2) (2018).
[17] M. Targoszkorecka, G.D. Brzezinka, K.E. Malek, E. Stępień, M. Szymonski, Stiffness memory of EA.hy926 endothelial cells in response to chronic hyperglycemia, Cardiovasc. Diabetol. 12 (1) (2013) 96.
[18] P. Lacolley, V. Regnault, P. Segers, S. Laurent, Vascular smooth muscle cells and arterial stiffening: relevance in development, aging, and disease, Physiol. Rev. 97 (4) (2017) 1555.
[19] D.F. Williams, On the nature of biomaterials, Biomaterials 30 (30) (2009) 5897–5909.
[20] F. Berthiaume, T.J. Maguire, M.L. Yarmush, Tissue engineering and regenerative medicine: history, progress, and challenges, Ann. Rev. Chem. Biomol. Eng. 2 (2) (2011) 403–430.
[21] E.S. Place, N.D. Evans, M.M. Stevens, Complexity in biomaterials for tissue engineering, Nat. Mater. 8 (6) (2009) 457–470.

[22] M. Lee, B.M. Wu, J.C. Dunn, Effect of scaffold architecture and pore size on smooth muscle cell growth, J. Biomed. Mater. Res. Part A 87A (4) (2010) 1010–1016.
[23] P. Thevenot, W. Hu, L. Tang, Surface chemistry influences implant biocompatibility, Curr. Top. Med. Chem. 8 (4) (2008) 270–280.
[24] E. Mazza, A.E. Ehret, Mechanical biocompatibility of highly deformable biomedical materials, J. Mech. Behav. Biomed. Mater. 48 (2015) 100–124.
[25] R. Monika, W. Alexander, J.W.C. Dunlop, D.J.T. Van, F. Peter, The effect of geometry on three-dimensional tissue growth, J. R. Soc. Interface 5 (27) (2008) 1173–1180.
[26] P. Stenlund, M. Trobos, J. Lausmaa, R. Brånemark, P. Thomsen, A. Palmquist, Effect of load on the bone around bone-anchored amputation prostheses, J. Orthop. Res. 35 (5) (2017) 1113–1122.
[27] H. Jo, M. Sim, S. Kim, S. Yang, Y. Yoo, J.H. Park, Y.T. Ho, M.G. Kim, L.J. Young, Electrically conductive graphene/polyacrylamide hydrogels produced by mild chemical reduction for enhanced myoblast growth and differentiation, Acta Biomater. 48 (2016) 100–109.
[28] A.J. Keung, E.M. de JuanPardo, D.V. Schaffer, S. Kumar, Rho GTPases mediate the mechanosensitive lineage commitment of neural stem cells, Stem Cells 29 (11) (2011) 1886–1897.
[29] J.H. Wen, L.G. Vincent, F. Alexander, C.Y. Suk, H. Kolin, T.W. Hermes, S. Chen, A. J. Engler, Interplay of matrix stiffness and protein tethering in stem cell differentiation, Nat. Mater. 13 (10) (2014) 979–987.
[30] E.Y. Tokuda, J.L. Leight, K.S. Anseth, Modulation of matrix elasticity with PEG hydrogels to study melanoma drug responsiveness, Biomaterials 35 (14) (2014) 4310–4318.
[31] M. Sheikholeslam, S.D. Wheeler, K.G. Duke, M. Marsden, M. Pritzker, P. Chen, Peptide and peptide-carbon nanotube hydrogels as scaffolds for tissue & 3D tumor engineering, Acta Biomater. (2018) 107–119.
[32] R. Neff, A. Adedeji, C.W. Macosko, A.J. Ryan, Urea hard segment morphology in flexible polyurethane foam, J. Polym. Sci. Part B-Polym. Phys. 36 (4) (1998) 573–581.
[33] A. Shababdoust, M. Ehsani, P. Shokrollahi, M. Zandi, Fabrication of curcumin-loaded electrospun nanofiberous polyurethanes with anti-bacterial activity, Prog. Biomater. 7 (1) (2018) 23–33.
[34] R.G.J.C. Heijkants, C.R.V. Van, T.T.G. Van, G.J.H. De, A.J. Pennings, P. Buma, R.P.H. Veth, A.J. Schouten, Polyurethane scaffold formation via a combination of salt leaching and thermally induced phase separation, J. Biomed. Mater. Res. Part A 87A (4) (2008) 921–932.
[35] M.A. Hood, B. Wang, J.M. Sands, J.J.L. Scala, F.L. Beyer, C.Y. Li, Morphology control of segmented polyurethanes by crystallization of hard and soft segments, Polymer 51 (10) (2010) 2191–2198.
[36] Q. Chen, S. Liang, G.A. Thouas, Elastomeric biomaterials for tissue engineering, Prog. Polym. Sci. 38 (3–4) (2013) 584–671.
[37] M. Mazurek-Budzyńska, M.Y. Razzaq, K. Tomczyk, G. Rokicki, M. Behl, A. Lendlein, Poly(carbonate-urea-urethane) networks exhibiting high-strain shape-memory effect, Polym. Adv. Technol. 28 (10) (2017) 1285–1293.
[38] R.Y. Kannan, H.J. Salacinski, M. Odlyha, P.E. Butler, A.M. Seifalian, The degradative resistance of polyhedral oligomeric silsesquioxane nanocore integrated polyurethanes: an in vitro study, Biomaterials 27 (9) (2006) 1971–1979.
[39] M.D. Hager, S. Bode, C. Weber, U.S. Schubert, Shape memory polymers: past, present and future developments, Prog. Polym. Sci. 49–50 (2015) 3–33.
[40] A. Lendlein, M. Behl, B. Hiebl, C. Wischke, Shape-memory polymers as a technology platform for biomedical applications, Expert Rev. Med. Devices 7 (3) (2010) 357–379.
[41] N. NIBIB, Memory foam for vascular treatment receives FDA clearance, July 19 2018. https://www.nibib.nih.gov/news-events/newsroom/memory-foam-vascular-treatment-receives-fda-clearance. (Accessed 07.08.18).
[42] S. Agarwal, J.H. Wendorff, A. Greiner, Use of electrospinning technique for biomedical applications, Polymer 49 (26) (2008) 5603–5621.
[43] R.C. Dutta, M. Dey, A.K. Dutta, B. Basu, Competent processing techniques for scaffolds in tissue engineering, Biotechnol. Adv. 35 (2) (2017) 240–250.
[44] N. Sultana, M. Wang, Fabrication of HA/PHBV composite scaffolds through the emulsion freezing/freeze-drying process and characterisation of the scaffolds, J. Mater. Sci.-Mater. Med. 19 (7) (2008) 2555.
[45] R. Scaffaro, F. Sutera, F. Lopresti, Using Taguchi method for the optimization of processing variables to prepare porous scaffolds by combined melt mixing/particulate leaching, Mater. Des. 131 (2017) 334–342.
[46] B. Derby, Printing and prototyping of tissues and scaffolds, Science 338 (6109) (2012) 921–926.
[47] K.R. Hixon, A.M. Melvin, A.Y. Lin, A.F. Hall, S.A. Sell, Cryogel scaffolds from patient-specific 3D-printed molds for personalized tissue-engineered bone regeneration in pediatric cleft-craniofacial defects, J. Biomater. Appl. 32 (5) (2017) 598–611.
[48] S.E. Bakarich, R. Gorkin, M.I.H. Panhuis, G.M. Spinks, 4D printing with mechanically robust, thermally actuating hydrogels, Macromol. Rapid Commun. 36 (12) (2015) 1211–1217.
[49] A.S. Gladman, E.A. Matsumoto, R.G. Nuzzo, L. Mahadevan, J.A. Lewis, Biomimetic 4D printing, Nat. Mater. 15 (4) (2016) 413–418.
[50] A.G. Kidane, G. Burriesci, M. Edirisinghe, H. Ghanbari, P. Bonhoeffer, A.M. Seifalian, A novel nanocomposite polymer for development of synthetic heart valve leaflets, Acta Biomater. 5 (7) (2009) 2409–2417.
[51] G. Kim, S. Ahn, H. Yoon, Y. Kim, W. Chun, A cryogenic direct-plotting system for fabrication of 3D collagen scaffolds for tissue engineering, J. Mater. Chem. 19 (46) (2009) 8817–8823.
[52] Y. Liang, X. Zheng, W. Zhai, T. Sun, 3D PLLA/nano-hydroxyapatite scaffolds with hierarchical porous structure fabricated by low-temperature deposition manufacturing, J. Wuhan Univ. Technol. (Mater. Sci. Ed.) 27 (2) (2012) 265–269.
[53] R. Hernandez-Cordova, D.A. Mathew, R. Balint, H.J. Carrillo-Escalante, J.M. Cervantes-Uc, L.A. Hidalgo-Bastida, F. Hernandez-Sanchez, Indirect three-dimensional printing: a method for fabricating polyurethane-urea based cardiac scaffolds, J. Biomed. Mater. Res. Part A 104 (8) (2016) 1912–1921.
[54] R. Akbarzadeh, J.A. Minton, C.S. Janney, T.A. Smith, P.F. James, A.M. Yousefi, Hierarchical polymeric scaffolds support the growth of MC3T3-E1 cells, J. Mater. Sci.-Mater. Med. 26 (2) (2015) 116.
[55] S. Mohanty, L.B. Larsen, J. Trifol, P. Szabo, H.V. Burri, C. Canali, M. Dufva, J. Emnéus, A. Wolff, Fabrication of scalable and structured tissue engineering scaffolds using water dissolvable sacrificial 3D printed moulds, Mater. Sci. Eng., C 55 (2015) 569–578.
[56] L. Onsager, Reciprocal relations in irreversible processes. I, Phys. Rev. 38 (37) (1931) 405–426.
[57] M.L. Huggins, Solutions of long chain compounds, J. Chem. Phys. 9 (5) (1941) 440.
[58] P.J. Flory, Thermodynamics of high polymer solutions, J. Chem. Phys. 9 (8) (1941) 660.
[59] R.G.J.C. Heijkants, R.V. van Calck, T.G. van Tienen, J.H. de Groot, A.J. Pennings, P. Buma, R.P.H. Veth, A.J. Schouten, Polyurethane scaffold formation via a combination of salt leaching and thermally induced phase separation, J. Biomed. Mater. Res. Part A 87A (4) (2008) 921–932.
[60] M. Behl, M.Y. Razzaq, A. Lendlein, Multifunctional shape-memory polymers, Adv. Mater. 22 (31) (2010) 3388–3410.
[61] M. Mazurek-Budzynska, M.Y. Razzaq, K. Tomczyk, G. Rokicki, M. Behl, A. Lendlein, Poly(carbonate-urea-urethane) networks exhibiting high-strain shape-memory effect, Polym. Adv. Technol. 28 (10) (2017) 1285–1293.